

# Inferring the Mean Effective Elastic Thickness of the Outer Ice Shell of Enceladus from Diurnal Crustal Deformation

Alexander Berne<sup>1</sup>, Mark Simons<sup>1</sup>, James Tuttle Keane<sup>2</sup>, Ryan S. Park<sup>2</sup>

<sup>1</sup>California Institute of Technology, Pasadena, CA 91125 USA

<sup>2</sup>Jet Propulsion Laboratory, California Institute of Technology, Pasadena, CA 91109 USA

## Key Points:

- Faults, crustal weak zones, and ice shell thickness variations affect how Enceladus responds to tidal forcing.
- Structural heterogeneities complicate inferring ice shell thickness using diurnal Love numbers.
- Measurements of tidal deformation at Enceladus would be a powerful probe of sub-surface structure.

## Abstract

The thickness of the outer ice shell plays an important role in several geodynamical processes at ocean worlds. Here we show that observations of tidally-driven diurnal surface displacements can constrain the mean effective elastic thickness,  $\tilde{d}_{el}$ , of the ice shell. Such estimates are sensitive to any significant structural features that break spherical symmetry such as faults and lateral variation in ice shell thickness and structure. We develop a finite-element model of Enceladus to calculate diurnal tidal displacements for a range of  $\tilde{d}_{el}$  values in the presence of such structural heterogeneities. We find that the presence of variations in ice shell thickness can significantly amplify deformation in thinned regions. If major faults are also activated by tidal forcing—such as Tiger Stripes on Enceladus—their characteristic surface displacement patterns could easily be measured using modern geodetic methods. Within the family of Enceladus models explored, estimates of  $\tilde{d}_{el}$  that assume spherical symmetry a priori can deviate from the true value by as much as  $\sim 20\%$  when structural heterogeneities are present. Such uncertainty is smaller than that found with approaches that rely on static gravity and topography ( $\sim 250\%$ ) or analyzing diurnal libration amplitudes ( $\sim 25\%$ ) to infer  $\tilde{d}_{el}$  at Enceladus. As such, despite the impact of structural heterogeneities, we find that analysis of diurnal tidal deformation is a relatively robust approach to inferring  $\tilde{d}_{el}$ .

## Plain Language Summary

For ocean worlds such as Enceladus, it is useful to determine the thicknesses of the outer ice crust—as it determines the depth of the ocean, the thermal evolution of the body, and the rate at which material at the surface can be recycled to the ocean. Here we show that the mean effective elastic thickness of the ice crust can be inferred from measuring the deformation of the surface in response to tidal forces. We also demonstrate that the presence of large fault systems (such as the Tiger Stripes) or variations in the thickness of the ice crust affect Enceladus’s response to tides.

## 1 Introduction

Enceladus, a moon orbiting Saturn approximately every 32.9 hrs, is demonstratively geologically active (Porco et al., 2006; Spencer et al., 2006; Hansen et al., 2006; Ingersoll et al., 2020). Erupting jets at the body’s surface align with the position of four promi-

44 nent, evenly spaced surface fractures (informally known as ‘Tiger Stripes’ (Porco et al.,  
 45 2006)). These fractures produce jets or geysers that are the source of a water-ice-dominated  
 46 plume emanating from the South Polar Terrain (SPT). The Tiger Stripes correlate with  
 47 the position of anomalously high heat flux and regional thinning at the SPT (Spencer  
 48 et al., 2006; Porco et al., 2014). Moreover, jet activity varies with orbital phase to pro-  
 49 duce maxima in plume brightness near orbital apoapse and periapse (Ingersoll et al., 2020).  
 50 The correlation of period of plume brightness oscillation period and Enceladus’s orbital  
 51 period strongly suggests that diurnal tides regulate heat and mass transport in the outer  
 52 ice shell (Hurford et al., 2007). We explore the interactions between crustal structure and  
 53 diurnal deformation to improve our understanding of the interior dynamics of Enceladus.

54 Constraints on ice shell structure, in particular outer shell mean thickness  $\tilde{d}_{ice}$ , pro-  
 55 vide a first-order constraint on the thermal properties, interior structure, and potential  
 56 for habitability of any ocean world.  $\tilde{d}_{ice}$  is an essential parameter for understanding the  
 57 total heat budget (Roberts & Nimmo, 2008), the potential for convection within the ice  
 58 shell (Mitri & Showman, 2005), the radial extent of the core and ocean (Hemingway &  
 59 Mittal, 2019), and the rate at which oxidized material cycles between the surface and  
 60 the ocean (Zolotov & Shock, 2004).  $\tilde{d}_{ice}$  also constrains plausible tidal heating mecha-  
 61 nisms on Enceladus including viscous dissipation in the crust (Souček et al., 2019) and  
 62 turbulent ocean flow (Hay & Matsuyama, 2019; Tyler, 2020).

63 Several approaches currently exist to infer  $\tilde{d}_{ice}$ . Static gravity and topography ad-  
 64 mittance modelling (Iess et al., 2014; McKinnon, 2015; Hemingway & Mittal, 2019; Ak-  
 65 iba et al., 2022) and diurnal shell libration amplitude measurements (Thomas et al., 2016)  
 66 yield estimates of  $\tilde{d}_{ice}$  for Enceladus between 17–60 km ( $\sim 250\%$ ) and 21–26 km ( $\sim 25\%$ )  
 67 respectively. These methods rely on the presence of large-scale non-hydrostatic surface  
 68 topography and a hydrostatic core, or alternatively, an orbital period comparable to the  
 69 resonant frequency of the ice shell (less than a few days). Here, we explore an alterna-  
 70 tive approach that relies on the analysis of the response to short-period (i.e., diurnal)  
 71 tidal forcing. Inferences of mean effective elastic thickness of the outer ice shell,  $\tilde{d}_{el}$ , from  
 72 analysis of diurnal tides are relatively insensitive to assumptions regarding the core and  
 73 are not contingent upon fortuitous structural or orbital conditions. The elastic behav-  
 74 ior of ice is also largely insensitive to temperature (i.e., elastic moduli vary  $< \pm 15\%$  across  
 75 crustal temperatures  $T = 70 - 273^\circ\text{K}$ ; Shaw, 1985; Neumeier, 2018) and so inferences  
 76 of  $\tilde{d}_{el}$  from diurnal tides closely approximate estimates of  $\tilde{d}_{ice}$  at Enceladus.

Differential gravitational attraction to a central, parent body (e.g., a planet) produces tides on orbiting satellites. Over timescales substantially greater than that of the orbital period (i.e., long-period), satellites deform as viscous fluids and the ultimate response to tidal forces is sensitive to radially varying internal density structure (e.g., Hubbard & Anderson, 1978). Bodies with eccentric orbits around their parent bodies experience an additional tidal force (i.e., the eccentricity or diurnal tide) which operates at a period equal to that of the orbit. At this timescale, any non-fluid interior layers may deform viscoelastically. For ocean-world bodies (i.e., where the outer ice shell and silicate core are mechanically decoupled by an intervening liquid ocean) deflection of the outer shell in response to diurnal tides is then relatively insensitive to the deep internal structure but is highly sensitive to  $\tilde{d}_{el}$ . Measurement of time-varying gravity or surface displacement can therefore be used to directly infer  $\tilde{d}_{el}$ .

The radial response of a body to time-dependent forcing can be described using gravitational and shape Love numbers  $k_l, h_l$  that depend on spherical harmonic degree  $l$  (Love, 1909). The  $l = 2$  diurnal Love numbers  $k_2^d$  and  $h_2^d$  track the very long-wavelength elastic response of bodies to diurnal tides and are sensitive to long-wavelength elastic structure (i.e.,  $\tilde{d}_{el}$ ). We will demonstrate that there only exists a unique relationship between a body's response and a load at  $l = 2$  for the limiting case of a fully spherically symmetric body. More generally, inferences of  $\tilde{d}_{el}$  from diurnal Love numbers at Enceladus requires accounting for the potential impact of non-spherically symmetric structure.

For an arbitrary 3D structure, we can formulate a general linear relationship between spherical harmonics  $V_{lm}$  (i.e., of degree  $l$  and order  $m$ ) of a driving gravitational potential  $V(\bar{\Omega})$  which deforms (i.e., drives mass movement) within a body generating harmonics  $U_{l'm'}$  of an induced gravitational potential  $U(\bar{\Omega})$ :

$$V(\bar{\Omega}) = \sum_{l=0}^{\infty} \sum_{m=-l}^l V_{lm} Y_{lm}(\bar{\Omega}) \quad (1a)$$

$$U(\bar{\Omega}) = \sum_{l'=0}^{\infty} \sum_{m'=-l'}^{l'} U_{l'm'} Y_{l'm'}(\bar{\Omega}) \quad (1b)$$

where  $Y_{lm}(\bar{\Omega})$  denote real spherical harmonics, the prime (') denotes induced components, and  $\bar{\Omega}$  is the position variable comprising a co-latitude and longitude pair  $(\theta, \phi)$  (Note: we restrict our analysis to the induced gravitational response but could easily apply the



methodology discussed in this section to derive the induced topographic response). For a linear elastic solid, deformation is linearly related to forcing (see also Supplementary S1.1). The tidal forcing harmonics  $V_{lm}$  accordingly map to harmonics  $U_{l'm'}$  via linear Green's functions  $\gamma_{lm}^{l'm'}$  which describe the elastic structure of a body:

$$\begin{bmatrix} U_{l'm'} \\ \vdots \\ \vdots \\ U_{\infty\infty} \end{bmatrix} = \begin{bmatrix} \gamma_{lm}^{l'm'} & \cdots & \cdots & \gamma_{\infty\infty}^{l'm'} \\ \vdots & \ddots & & \vdots \\ \vdots & & \ddots & \vdots \\ \gamma_{lm}^{\infty\infty} & \cdots & \cdots & \gamma_{\infty\infty}^{\infty\infty} \end{bmatrix} \begin{bmatrix} V_{lm} \\ \vdots \\ \vdots \\ V_{\infty\infty} \end{bmatrix} \quad (2)$$

Equation 2 demonstrates that  $U_{l'm'}$  depends on both  $\gamma_{lm}^{l'm'}$  and combinations of  $V_{lm}$ . In other words, the response of a body (i.e., at  $l'm'$ ) will vary according to the changing shape of an applied load *despite* a fixed elastic structure. For diurnal tides, the driving potential is comprised of three harmonics  $V_{20}$ ,  $V_{22}$ , and  $V_{2-2}$  (Murray & Dermott, 1999) and Equation 2 simplifies to:

$$\begin{bmatrix} U_{l'm'} \\ \vdots \\ \vdots \\ U_{\infty\infty} \end{bmatrix} = \begin{bmatrix} \gamma_{20}^{l'm'} & \gamma_{22}^{l'm'} & \gamma_{2-2}^{l'm'} \\ \vdots & \vdots & \vdots \\ \vdots & \vdots & \vdots \\ \gamma_{20}^{\infty\infty} & \gamma_{22}^{\infty\infty} & \gamma_{2-2}^{\infty\infty} \end{bmatrix} \begin{bmatrix} V_{20} \\ V_{22} \\ V_{2-2} \end{bmatrix} \quad (3)$$

$U_{l \neq 2m} \neq 0$  indicate a coupling between forcing and response across spatial scales (i.e., ‘mode coupling’; Dahlen & Tromp, 1998). To derive Love numbers, we restrict our analysis to the  $U_{20}$ ,  $U_{22}$ , and  $U_{2-2}$  components of the induced gravitational potential field. Equation 3 then simplifies to:

$$\begin{bmatrix} U_{20} \\ U_{22} \\ U_{2-2} \end{bmatrix} = \begin{bmatrix} \gamma_{20}^{20} & \gamma_{22}^{20} & \gamma_{2-2}^{20} \\ \gamma_{20}^{22} & \gamma_{22}^{22} & \gamma_{2-2}^{22} \\ \gamma_{20}^{2-2} & \gamma_{22}^{2-2} & \gamma_{2-2}^{2-2} \end{bmatrix} \begin{bmatrix} V_{20} \\ V_{22} \\ V_{2-2} \end{bmatrix} \quad (4)$$

The individual components  $\gamma_{lm}^{l'm'}$  in Equation 4 contain information regarding the sphericity of a body's elastic structure. For a non-rigid body, diagonal components (i.e.,  $\gamma_{20}^{20}, \gamma_{22}^{22}, \gamma_{2-2}^{2-2}$ ) are always non-zero and are principally sensitive to bulk elastic properties (e.g.,  $\tilde{d}_{el}$ ; Wahr et al., 2006). Off-diagonal components (i.e.,  $\gamma_{22}^{20}, \gamma_{20}^{22}, \gamma_{2-2}^{22}, \gamma_{22}^{2-2}, \gamma_{20}^{2-2}, \gamma_{2-2}^{20}$ ) represent coupling between forcing and response at mutually distinct harmonics. At spatial wavelengths significantly greater than  $\tilde{d}_{el}$ , the outer ice crust of spherically symmetric ocean worlds

conform to the shape of driving potential surfaces (i.e., following the thin-plate approximation originally derived from beam theory; Levinson, 1984). According to Equation 4, distinct diagonal components or non-zero off-diagonal components therefore imply the presence of non-spherically symmetric structure. For a spherically symmetric body,  $\gamma_{22}^{20} = \gamma_{20}^{22} = \gamma_{2-2}^{22} = \gamma_{2-2}^{20} = \gamma_{2-2}^{2-2} = \gamma_{20}^{2-2} = 0$  and  $\gamma_{20}^{20} = \gamma_{22}^{22} = \gamma_{2-2}^{2-2} = k_2^d$ . Equation 4 then simplifies to:

$$\begin{bmatrix} U_{20} \\ U_{22} \\ U_{2-2} \end{bmatrix} = \begin{bmatrix} k_2^d & 0 & 0 \\ 0 & k_2^d & 0 \\ 0 & 0 & k_2^d \end{bmatrix} \begin{bmatrix} V_{20} \\ V_{22} \\ V_{2-2} \end{bmatrix} \quad (5)$$

We can define ‘effective’ Love numbers  $k_{2m}^d$  as quantities which track  $U_{2m}$  normalized by  $V_{2m}$  (i.e.,  $k_{2m} = U_{2m}/V_{2m}$ ) for an  $l = 2$  driving potential with an arbitrary overall shape. According to Equation 5, a unique relationship between harmonics  $U_{2m}$  and  $V_{2m}$  exists only for spherically symmetric structures (i.e.,  $k_{2m} \rightarrow k_2$ ). More generally,  $k_{2m}^d$  are sensitive to non-spherically symmetric structure and the overall shape of the load (i.e.,  $V_{20}$ ,  $V_{22}$ , and  $V_{2-2}$ ) such that  $k_{20} \neq k_{22} \neq k_{2-2}$  (i.e., ‘order splitting’ or ‘spectral leakage’) (Behoukova et al., 2017; Ermakov et al., 2021; Vance et al., 2021). Several structures are expected to break spherical symmetry at Enceladus including lateral variations in thickness of the ice shell, structurally weak (e.g., highly fractured or damaged) zones, or the presence of major fault structures (Behoukova et al., 2017). We therefore expect that diurnal Love numbers are not directly sensitive to  $\tilde{d}_{el}$  at Enceladus and inferences of  $\tilde{d}_{el}$  from  $k_{2m}^d$  should account for the potential influence of structural heterogeneities in the outer ice crust.

Several studies describe the relationship between elastic structure and diurnal deformation at Enceladus. Wahr et al., (2006) develop analytic expressions to calculate  $k_{2m}^d$  and  $h_{2m}^d$  from eccentricity tides at ocean worlds using an approach that only applies to spherically symmetric models. Beuthe (2018) extends this analysis of  $k_{2m}^d$  and  $h_{2m}^d$  to allow for variations in crustal thickness but assumes a thin-shelled approximation and does not include the potential impact of faults. The most sophisticated models to date by Souček et al., (2016), Behoukova et al., (2017), and Souček et al., (2019) simulate deformation using finite-element models (FEM) of the outer ice shell with both variations in ice thickness and weak zones. These studies do not specifically address the relationship between deformation and  $\tilde{d}_{el}$  and exclude effects from a broader range of struc-

tural heterogeneities inferred from surface geology at Enceladus including large circum-tectonic boundaries and extensional fractures extending radially outward from the South Polar Terrain (i.e., chasma).

Here, we explore how estimates of  $\tilde{d}_{el}$ , based on analysis of diurnal tides, are potentially impacted by structural heterogeneities within the ice crust of Enceladus. We simulate deformation on tidally-loaded quasi-spherical shells using a FEM and compare results from five sets of end member models of Enceladus: (1) A spherically symmetric ice shell; (2) An ice shell with variations in thickness; (3) An ice shell with faults; (4) An ice shell with both variations in thickness and faults; and (5) An ice shell with faults, variations in thickness, and ‘weak zones’ (regions of reduced shear modulus) at locations corresponding to the position of additional structures inferred from Enceladus’s geology (i.e., chasma and circum-tectonic boundaries). We parameterize the response of the shell by calculating  $k_{20}^d$ ,  $k_{22}^d$ ,  $k_{2-2}^d$  and  $h_{20}^d$ ,  $h_{22}^d$ ,  $h_{2-2}^d$ , from deformed geometries and compare these predicted values with those predicted from models without structural heterogeneities. We then explore the challenge associated inferring  $\tilde{d}_{el}$  from  $k_{20}^d$  and  $h_{20}^d$ ,  $k_{22}^d$  and  $h_{22}^d$ , or  $h_{22}^d$  and  $k_{2-2}^d$  posed by the presence of structural heterogeneities in the crust. We conclude by highlighting the potential for analyzing diurnal tides to determine  $\tilde{d}_{el}$  both for Enceladus as well as for other ocean worlds.

## 2 Methods

We develop a quasi-spherical FEM of Enceladus that allows for structural heterogeneities in the ice shell and that can be used to predict the elastic response of the body to diurnal tidal loads. We first build an FEM mesh that reflects desired structural heterogeneities. We then use a modified version of the finite-element code Pylith (Aagaard et al., 2007) to calculate displacements on models subjected to tidal forcing. In post-processing, we extract  $l = 2$  Love numbers from model displacements. We describe each of these steps in detail below.

### 2.1 Model Preparation

We consider five types of models that differ in the style of structural heterogeneity assumed: (1) a *Base* model without structural heterogeneities; (2) a model with large scale faults (a.k.a. *Faulted*); (3) a model with Lateral Thickness Variations (a.k.a. *LTV*);

(4) a combined model (a.k.a. *Faulted+LTV*); and (5) a combined model with additional weak zones at locations coincident with major geologic structures (a.k.a. *Faulted+LTV+WZ*). For each model, we develop a mesh with tetrahedral elements using the software package CUBIT (Skroch et al., 2019; CoreForm, 2020) and refine cell size in regions which locally exhibit high strain (e.g., near faults). We perform a mesh convergence test to verify our choice of element sizing parameters provide accurate Love number values on models with structural heterogeneities (see supplementary section S1.3).

- For the *Base* models, we mesh a spherical shell with a specified input thickness  $\tilde{d}_{el}$ . All of our models have baseline elastic parameters consistent with the rheology of ice (Jaccard, 1976; Shaw, 1985; Neumeier, 2018). We assign a base shear modulus value for ice of  $G = 3.3$  GPa and a bulk modulus of  $\mu = 8.6$  GPa (i.e., consistent with the formulation described in Souček et al., (2016) with  $G = 3.3$  GPa and Poisson’s ratio  $\nu = 0.33$ ). For this analysis, we ignore viscous effects since viscous strain at the forcing period relevant for Enceladus (33 hours) is expected to be negligibly small ( $<0.1\%$  of the total shell strain (Wahr et al., 2009), see also Supplementary Section S1.2). Short-period elastic deformation of the core is also expected to be several orders of magnitude smaller than shell deformation (Schubert et al., 2007), thus we treat the core as a rigid body and ignore any impact deformation of the core may have on the response of the ice shell to eccentricity tides.
- For the *Faulted* models, we introduce fault surfaces that are through-going (i.e., they extend through the full thickness of the ice-shell) and are frictionless. Motion across these faults is restricted to shear with no opening. The explicit inclusion of fault surfaces within the FEM formulation uses a ‘split-node’ formulation whereby we duplicate nodes along the fault plane and introduce special cohesive cells between node sets (Melosh & Raefsky, 2009). Split-node formulations allow for robust calculations of fault-induced deformation and self-consistent predictions of fault slip. Our *Faulted* model specifically refers to a shell with four faults at the south pole consistent with the mapped extent of Tiger Stripes at Enceladus. We extract the surface trace of the Tiger Stripes from existing maps of Enceladus (Schenk, 2008).

- To construct the *LTV* models, we apply topography,  $H_{top}$ , to the outer surface of our base model geometry and modify the inner surface (i.e., the ice-ocean boundary),  $H_{bottom}$ , assuming isostatic (Airy) compensation. Given surface gravitational acceleration  $g_0$ , outer shell ice of density  $\rho_{ice}$ , ocean water of density  $\rho_w$ , gravitational acceleration at the ice-ocean interface  $g_{int}$ , mean radius of the ice-ocean boundary  $R_{int}$ , and mean radius of the outer surface  $R_0$  (see Table 1 for chosen values of these parameters) (Hemingway & Matsuyama, 2017), we can write:

$$H_{bottom} = H_{top} \frac{\rho_{ice}}{(\rho_{ice} - \rho_w)} \frac{g_0}{g_{int}} \frac{R_0^2}{R_{int}^2} \quad (6)$$

**Table 1.** Assumed parameter values used in Equation 6. Parameter values taken from Schenk et al., (2018)

| Parameter    | Value | Units             |
|--------------|-------|-------------------|
| $\rho_{ice}$ | 925   | kg/m <sup>3</sup> |
| $\rho_w$     | 1007  | kg/m <sup>3</sup> |
| $g_0$        | 0.113 | m/s <sup>2</sup>  |
| $g_{int}$    | 0.120 | m/s <sup>2</sup>  |
| $R_0$        | 252.1 | km                |

Our *LTV* models use topography extracted from the shape model given by Nimmo et al. (2011) up to a maximum spherical harmonic degree  $L_{max} = 8$ . Our *Faulted+LTV* model includes both types of structural heterogeneities.

- Our *Faulted+LTV+WZ* models include additional through-going ‘weak zones’ at locations corresponding to the south polar circum-tectonic boundary, chasma, and Tiger Stripes. To generate weak zones, we assign material within 1-km wide zones to have an elastic shear modulus,  $G_{WZ}$ , reduced to  $10^{-5} G$  (i.e., while maintaining a constant bulk modulus and ice density). By lowering the shear modulus, we approximate the behavior of damaged regions of the ice shell (i.e., as opposed to creating split-node surfaces for slipping fault structures). For these models, Tiger Stripes include both surrounding weak zone volumes and split-node surfaces along the fault plane. We extract chasma and circum-tectonic boundary positions from locations described by Yin & Pappalardo (2008).

## 2.2 Tidal Loading

For Enceladus, the driving potential produced by time-dependent eccentricity tides at a point  $V(r, \theta, \phi)$  in an Enceladus-fixed frame (i.e., the  $(\theta = 90^\circ, \phi = 0^\circ)$  datum lies at the sub-Saturnian point, where  $\theta$  is co-latitude and  $\phi$  is longitude) is written as a combination of radial  $V_{rad}(r, \theta, \phi)$  and librational  $V_{lib}(r, \theta, \phi)$  terms (Murray & Dermott, 1999):

$$V_{rad}(r, \theta, \phi) = r^2 \omega^2 e \cdot \cos(\omega t) \frac{3}{4} (P_{22}(\mu) \cos 2\phi - 2 P_{20}(\mu)) \quad (7a)$$

$$V_{lib}(r, \theta, \phi) = r^2 \omega^2 e \cdot \sin(\omega t) P_{22}(\mu) \sin 2\phi \quad (7b)$$

Each term in Equation 7 is scaled by the factor  $\omega^2 e$ , where  $\omega = 5.307 \times 10^{-5} \text{ s}^{-1}$  is Enceladus's orbital angular velocity and  $e = 0.0047$  is the body's orbital eccentricity. Time  $t = 0, \frac{2\pi}{\omega}$  corresponds to orbital periapse.  $P_{20}(\mu)$  and  $P_{22}(\mu)$  are associated Legendre Functions with the nested function  $\mu = \cos(\theta)$ . We apply body forces, ocean tractions, topographic surface traction forces, and self-gravitational forces produced by the driving potential from Equation 7 and calculate displacement fields arising from these loads. We ignore inertial forces for our analysis (see Supplementary 1.1).

We use the 3D visco-elasto-plastic FEM code Pylith (Aagaard et al., 2008). Pylith is a well-established and extensively benchmarked tool developed in the terrestrial crustal dynamics community for studying tectonic processes on Earth. Pylith allows for complex bulk rheology, various formulations for fault behavior, and complex geometrical meshes. Pylith was originally designed for quasi-Cartesian problems; as such we have modified it to allow for modeling full spheres in a no-net-rotation/translation reference frame with central time-dependent body forces appropriate for eccentricity tides. We benchmark our tidal loading formulation as implemented in Pylith applied to our *Base* model against the program SatStress (Wahr et al., 2009) (see supplementary section S1.1-1.2).

## 2.3 Calculation of Love numbers

We post-process the resulting deformation fields to evaluate the  $l = 2$  diurnal Love numbers,  $k_{20}^d$ ,  $k_{22}^d$ , and  $k_{2-2}^d$  or  $h_{20}^d$ ,  $h_{22}^d$ , and  $h_{2-2}^d$ . The ‘diurnal’ Love numbers are distinct from ‘fluid’ Love numbers  $k_{20}^f$ ,  $k_{22}^f$ , and  $k_{2-2}^f$  or  $h_{20}^f$ ,  $h_{22}^f$ , and  $h_{2-2}^f$ . ‘Fluid’ Love numbers are sensitive to the arrangement of a body's interior layers which deflect in response to long-period static tides in order to achieve hydrostatic equilibrium (Goldreich & Mitchell, 2010). By contrast, diurnal Love numbers depend on the elastic response of the body

to short-period eccentricity tides (see Equation 7) and are superimposed onto the long-period tide. Moreover, diurnal Love numbers are usually at least an order of magnitude smaller than fluid Love numbers (Beuthe, 2018; Hemingway & Mittal, 2019). Relative to the fluid Love numbers, the diurnal Love numbers are less sensitive to deeper interior structure at ocean worlds (Wahr et al., 2009).

For  $h_{20}^d$ ,  $h_{22}^d$ , and  $h_{2-2}^d$  we expand the outer surface of our deformed geometry into spherical harmonics and separately compute the  $l = 2$  zonal and sectoral coefficients  $H_{20}$ ,  $H_{22}$ , and  $H_{2-2}$ . We calculate  $V_{20}$ ,  $V_{22}$ , and  $V_{2-2}$  using the  $l = 2$  components of the tidal potential from Equation 7:

$$V_{20} = -\frac{3}{2}r^2\omega^2e \cdot \cos(\omega t) \quad (8a)$$

$$V_{22} = \frac{3}{4}r^2\omega^2e \cdot \cos(\omega t) \quad (8b)$$

$$V_{2-2} = r^2\omega^2e \cdot \sin(\omega t) \quad (8c)$$

From  $V_{20}$ ,  $V_{22}$ ,  $V_{2-2}$ ,  $h_{20}^d$ ,  $h_{22}^d$ , and  $h_{2-2}^d$  and the definition of the Love numbers, we have:

$$h_{20}^d = g_0 H_{20} / V_{20} \quad (9a)$$

$$h_{22}^d = g_0 H_{22} / V_{22} \quad (9b)$$

$$h_{2-2}^d = g_0 H_{2-2} / V_{2-2} \quad (9c)$$

Following a similar procedure for  $k_{20}^d$ ,  $k_{22}^d$ , and  $k_{2-2}^d$ , we compute the  $l = 2$  sectoral and zonal coefficients  $U_{20}$ ,  $U_{22}$ , and  $U_{2-2}$  of the spherical harmonic expansion of the induced gravitational potential field (see Equation 1) associated with the deformed geometry:

$$k_{20}^d = U_{20} / V_{20} \quad (10a)$$

$$k_{22}^d = U_{22} / V_{22} \quad (10b)$$

$$k_{2-2}^d = U_{2-2} / V_{2-2} \quad (10c)$$

As mentioned earlier, Love numbers defined in this way will depend on the time-varying shape and amplitude of the driving potential (i.e., see Equations 4 and 8). Thus, we expect values of  $k_{20}^d$ ,  $k_{22}^d$ , and  $k_{2-2}^d$  or  $h_{20}^d$ ,  $h_{22}^d$ , and  $h_{2-2}^d$  to vary over the tidal cycle at Enceladus. Since we aim to minimize the impact of non-spherically symmetric structure on inferences of  $\tilde{d}_{el}$ , we evaluate deformation at two unique points in the tidal cycle:  $t =$

0 and  $t = \frac{\pi}{2\omega}$ . At  $t = 0$  (or  $\frac{\pi}{\omega}$ ),  $V_{2-2} = 0$  (according to Equation 8) which eliminates the potential impact of the off-diagonal components  $\gamma_{2-2}^{22}$ ,  $\gamma_{2-2}^{20}$ ,  $\gamma_{22}^{2-2}$ , and  $\gamma_{20}^{2-2}$  (from Equation 4) on values of  $k_{20}^d$  or  $k_{22}^d$ . Similarly, at  $t = \frac{\pi}{2\omega}$  (or  $\frac{3\pi}{2\omega}$ ),  $V_{20} = V_{22} = 0$  which eliminates the impact of all off-diagonal components on values of  $k_{2-2}^d$ .

## 2.4 Previous FEM Models

Our FEMs are similar to, but distinct from, those described in the papers Souček et al., (2016) and Behoukova et al., (2017). We employ a tidal forcing formulation which is identical to that described in Souček et al., (2016) to generate body, ocean traction, and topographic loading forces. However, we include the effect of self-gravitation in our models (which modifies final calculated values of  $k_{20}^d$ ,  $k_{22}^d$ , and  $k_{2-2}^d$  or  $h_{20}^d$ ,  $h_{22}^d$ , and  $h_{2-2}^d$  by up to 3%). Souček et al., (2016) employ weak (i.e., highly damaged) zones as proxies the behavior of fault interfaces. In contrast, we adopt a split-node approach at the fault-plane to simulate deformation which enables straightforward calculations of fault slip. Souček et al., (2016) and Behoukova et al., (2017) also focus on the implications of deformation for tidal heating, while we focus here on the inference of shell structural parameters in the presence of structural heterogeneities. Finally, our models additionally consider the effect of fault zones beyond the Tiger Stripes and thereby identify the extent to which other major structural heterogeneities (e.g., chasma and circum-tectonic boundaries) may affect diurnal deformation patterns at Enceladus.

The most significant difference between models by Souček et al., (2016) and those described in this work relates to respective formulations for weak zones. Whereas Souček et al. (2016) reduce shear modulus to effectively negligible values while maintaining a constant Poisson’s ratio within damaged regions, we formulate weak zones by locally reducing shear modulus and maintaining a constant bulk modulus. We choose to maintain a constant bulk modulus in weak zones since this formulation is consistent with the expected behavior of damaged ice permeated (or filled) by water (Kalyanaraman et al., 2020). (Note: we are able to largely reproduce the results of Souček et al., (2016) by employing weak zones only at Tiger Stripe locations and reducing both bulk and shear modulus to effectively negligible values, see Supplementary S1.2). Maintaining a constant bulk modulus allows weak zones to accommodate significant extensional and compressional strain and therefore substantially reduces displacements surrounding structural hetero-



geneities (e.g., the Tiger Stripes) relative to displacements from models by Souček et al., (2016) (See Figures 1 and Figure 2 in the Supplementary Documentation).

### 3 Results

Figures 1 and 2 show snapshots of the radial displacement fields from each of the five model classes. The upper panels show absolute displacements on our *Base* model whereas the subsequent panels show the radial displacement fields for models incorporating structural heterogeneities relative to our *Base* model. Not surprisingly, there is a substantial increase in localized deformation near zones of structural heterogeneities (i.e., consistent with model results from Souček et al., (2016) and Behouňková et al., (2017)). In the *LTV* model, the highest increases in displacement values occur near the South Pole where the ice shell is thinnest. In the *Faulted* model, radial displacements are maximum near fault tips (also at the South Pole) and follow a double-couple pattern characteristic of slip along these structures (e.g., Segall, 2010). We show example snapshots of fault slip along the Tiger Stripes evaluated on our *Faulted* model and crustal thickness variations in our *LTV* model in Figure 3. In our *Faulted+LTV+WZ* model, localized radial deformation is partitioned between the Tiger Stripes, chasma, and circum-tectonic boundaries in a complex manner with further increases in displacement near the Tiger Stripes due to extensional and shear strain localization along weak zones. Long-wavelength increases in displacement amplify values of the Love numbers for models incorporating structural heterogeneities. Moreover, surface deformation at this scale does not follow the pattern of the disturbing potential from Equation 7. This difference causes values of  $k_{20}^d$ ,  $k_{22}^d$ , and  $k_{2-2}^d$  (or  $h_{20}^d$ ,  $h_{22}^d$ , and  $h_{2-2}^d$ ) to diverge from each other (i.e., ‘order-splitting’).

Results for  $k_{20}^d$ ,  $h_{20}^d$ ,  $k_{2-2}^d$ , and  $h_{2-2}^d$  from each model category are shown in Figure 4. Note that all the non-spherically symmetric models have enhanced values of  $k_{20}^d$ ,  $h_{20}^d$ ,  $k_{2-2}^d$  and  $h_{2-2}^d$  across all  $\tilde{d}_{el}$  values consistent with the amplification of deformation shown in models with structural heterogeneities (see Figures 1 and 2). Figure 4 also shows the range of possible values of  $\tilde{d}_{el}$  (i.e.,  $\Delta\% \tilde{d}_{el}$ ) corresponding to individual  $k_{20}^d$  and  $h_{20}^d$  or  $k_{2-2}^d$  and  $h_{2-2}^d$  values when treating *Base* and selected models with structural heterogeneities as end member scenarios. Results similar to those shown in Figure 4 illustrating the behavior of  $k_{22}^d$  and  $h_{22}^d$  are shown in Figure 5. Note the distinct values of  $k_{22}^d$  and  $h_{22}^d$  compared to  $k_{20}^d$  and  $h_{20}^d$  or  $k_{2-2}^d$  and  $h_{2-2}^d$  (i.e., ‘order-splitting’) in models with structural

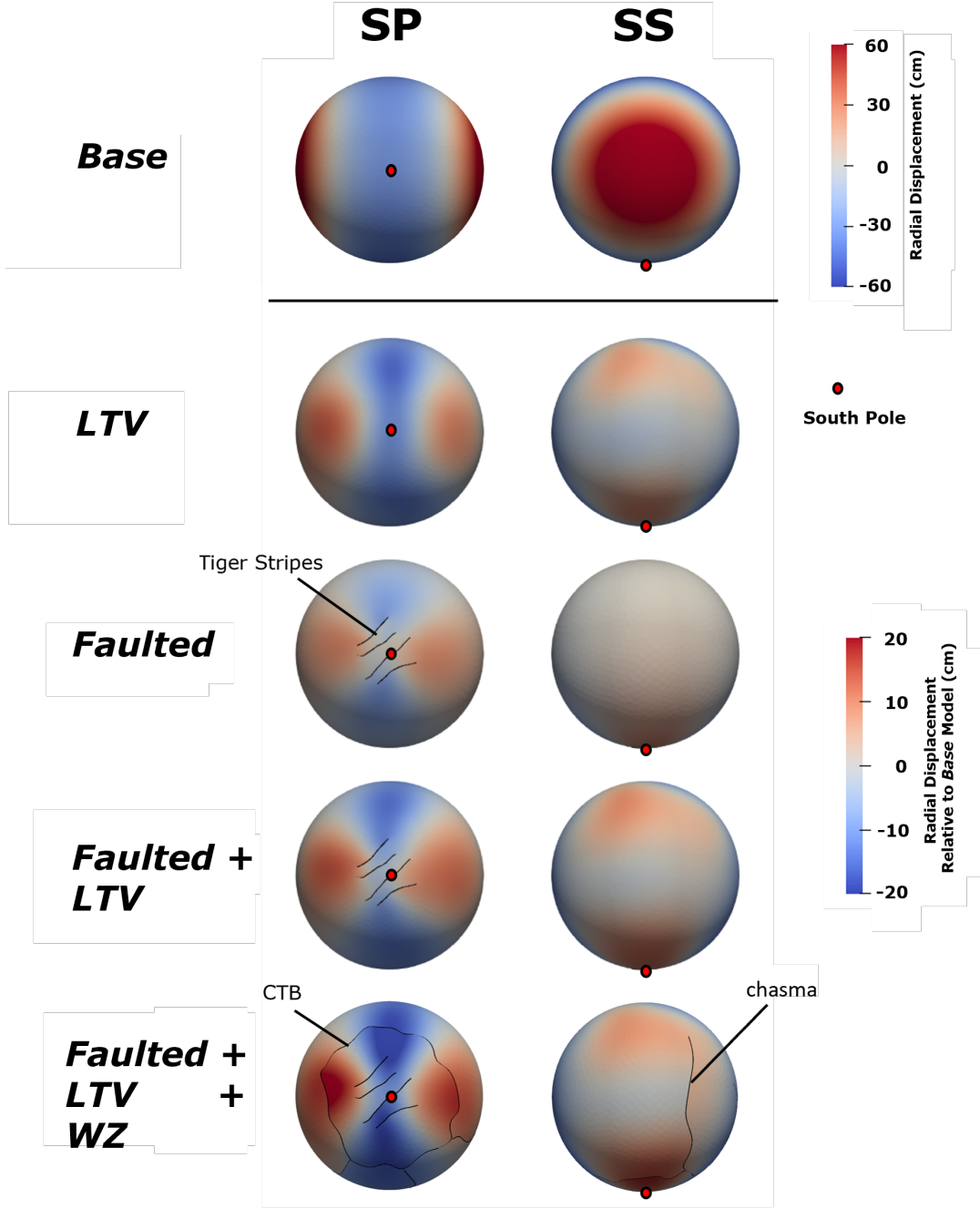


**Figure 1.** Snapshots of radial displacement from each model class viewed facing the south pole (SP, left column) and the sub-Saturnian point (SS, right column) evaluated at  $t = 0$  (periapse). The top row shows the radial displacement in the *Base* model due to tidal forcing. The remaining rows present the differences in radial displacement between models with structural heterogeneities and the *Base* model. Each model shown assumes  $\tilde{d}_{el} = 25$  km. Tiger Stripes, the south polar circum-tectonic boundary (CTB), and chasma are labelled. Figure 2 shows the same models at a different time in Enceladus’s orbit.

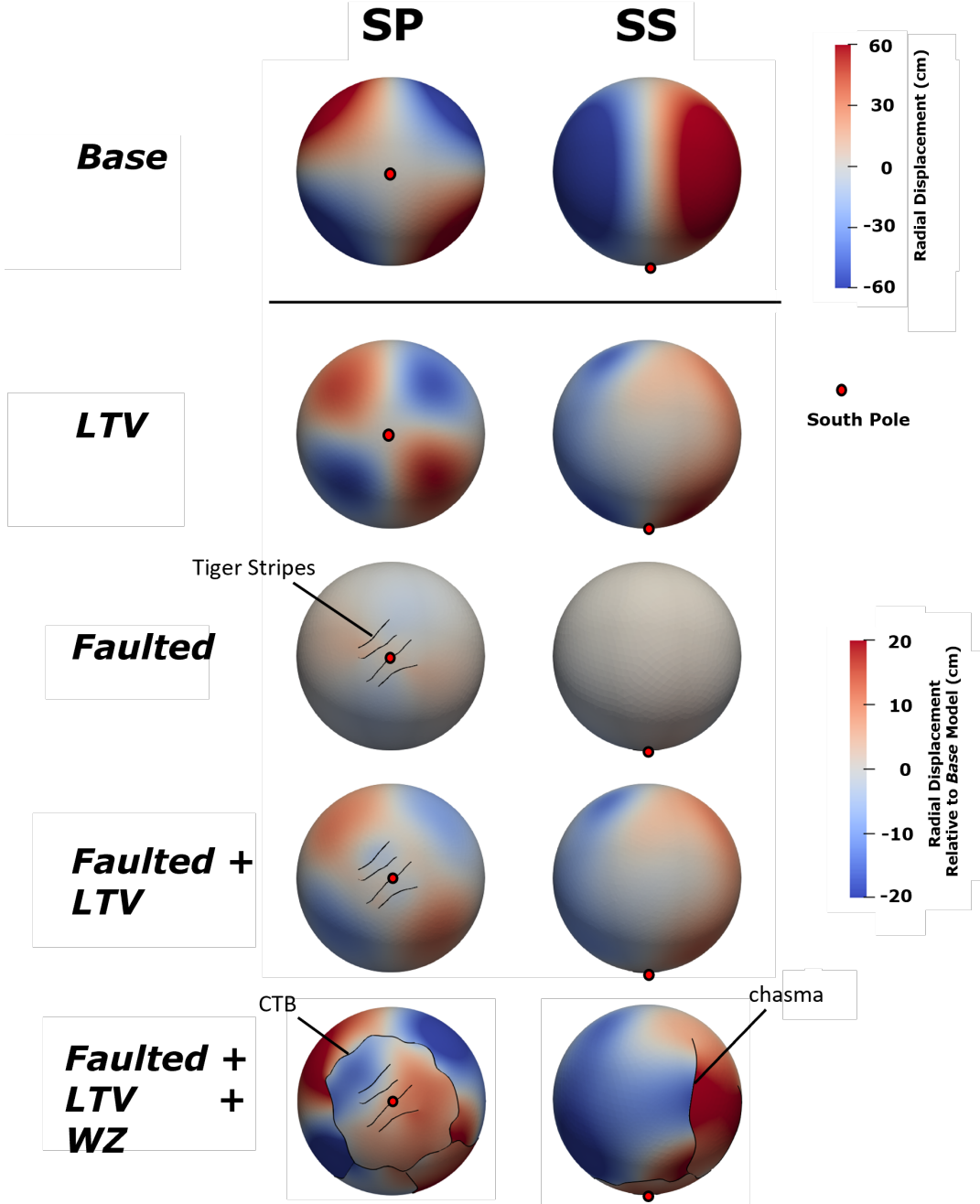


**Figure 2.** Snapshots of radial displacement from each model class viewed facing the south pole (SP, left column) and the sub-Saturnian point (SS, right column) evaluated at  $t = \frac{\pi}{2\omega}$ . The top row shows the radial displacement in the *Base* model due to tidal forcing. The remaining rows present the differences in radial displacement between models with structural heterogeneities and the *Base* model. Each model shown assumes  $\tilde{d}_{el} = 25$  km. Tiger Stripes, the south polar circum-tectonic boundary (CTB), and chasma are labelled. Figure 1 shows the same models at a different time in Enceladus’s orbit.

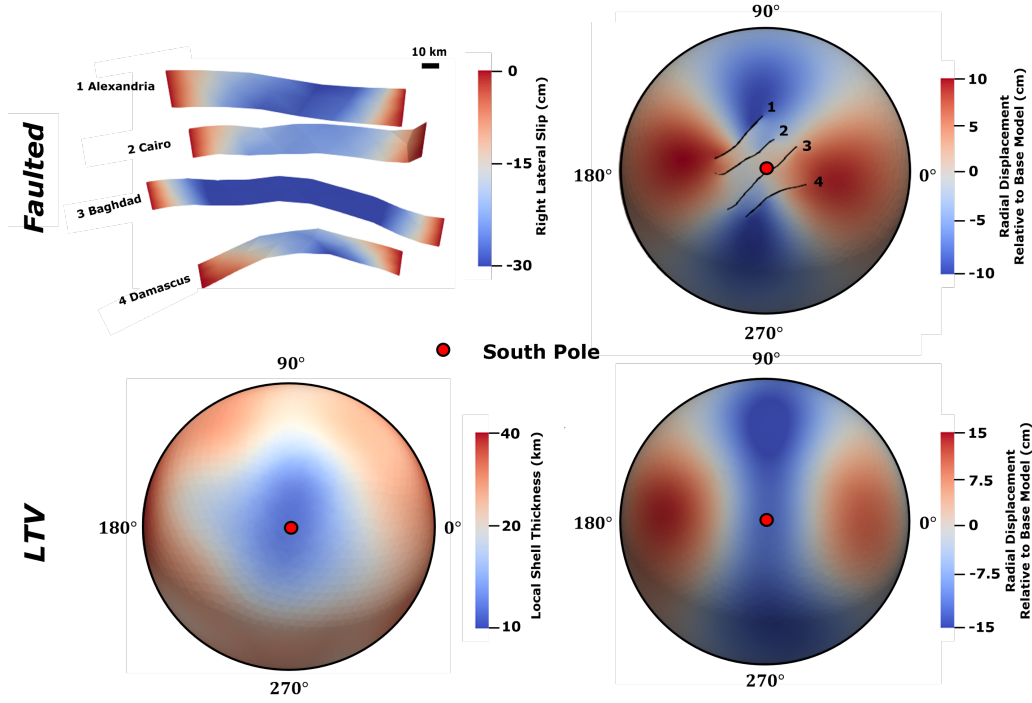


**Figure 3.** Snapshots of slip along the Tiger Stripes and regional thinning near the South Pole corresponding to deformation shown in *Faulted* (top row) and *LTV* (bottom row) models respectively in Figure 1. The upper left image shows a perspective view of fault slip on the Tiger Stripes, where negative (blue) values indicate left-lateral slip. The upper right shows a south polar projection (where  $0^\circ$  corresponds to the sub-Saturnian longitude), with fault locations overlaid on radial displacements (this is rescaled from the third row of Figure 1). The bottom row shows images of the crustal thickness variations (left) and a south polar projection showing radial displacements (right) evaluated from the *LTV* model (i.e., rescaled from the second row of Figure 1). Local thickness values are plotted in  $\log_{10}$  scale. Each model shown assumes  $\tilde{d}_{el} = 25$  km and is evaluated at  $t = 0$  (periapse).

heterogeneities. To directly quantify the impact of structural heterogeneities on order-splitting, we additionally plot values of  $k_{22}^d/k_{20}^d$  and  $h_{22}^d/h_{20}^d$  vs.  $\tilde{d}_{el}$  in Figure 5. We track  $k_{22}^d/k_{20}^d$  and  $h_{22}^d/h_{20}^d$  since these quantities implicitly account for the baseline impact of  $\tilde{d}_{el}$  on Love numbers and are especially sensitive to the presence of structural heterogeneities near the South Pole of Enceladus (See discussion).

## 4 Discussion and Conclusion

We evaluate the relationship between mean effective elastic thickness,  $\tilde{d}_{el}$ , and diurnal Love numbers for a range of shell models with structural heterogeneities. We find that structural heterogeneities broaden the range of possible  $\tilde{d}_{el}$  values corresponding to a measured Love number by about 41% in the most extreme case. The maximal range of plausible  $\tilde{d}_{el}$  values increases less than 30% for  $\tilde{d}_{el}$  values above 20 km (likely values of  $\tilde{d}_{el}$  at Enceladus are between 21–26 km; Thomas et al., 2016). Moreover, if weak zones are not present on Enceladus then the range of plausible  $\tilde{d}_{el}$  values further reduces to less than  $\sim 20\%$ .

The diurnal response of Enceladus to eccentricity tides is highly sensitive to variations in the thickness of the ice crust. *LTV* models show deviation in inferred  $\tilde{d}_{el}$  values relative to *Base* models of up to 18%. The amplification of deformation in thinned regions (see Figures 1 and 3) is highly dependent on  $\tilde{d}_{el}$ . As  $\tilde{d}_{el}$  approaches 15 km, effective elastic thickness approaches zero locally and strain increases rapidly near the South Pole. The resulting enhanced deformation drives the observed large increase in Love numbers at  $\tilde{d}_{el} < 20$  km (Figure 4 and 5).

As implemented here, faults have less impact on long-wavelength deformation than do variations in the thickness of the ice crust. Fault structures in isolation bias inferred  $\tilde{d}_{el}$  values from diurnal Love number values by up to 3%—rather insignificant. This observation follows from Figures 1 and 3 which shows that fault-induced deformation creates a strong double-couple deformation pattern as expected from slip on Tiger Stripes. Slip-induced deformation produces substantial radial displacement at scales comparable to the size of associated faults but reduced displacement at longer wavelengths. As such, for the Tiger Stripes along-fault slip only modestly increases diurnal Love number values. Moreover, we expect the influence of Tiger Stripe slip on diurnal love num-

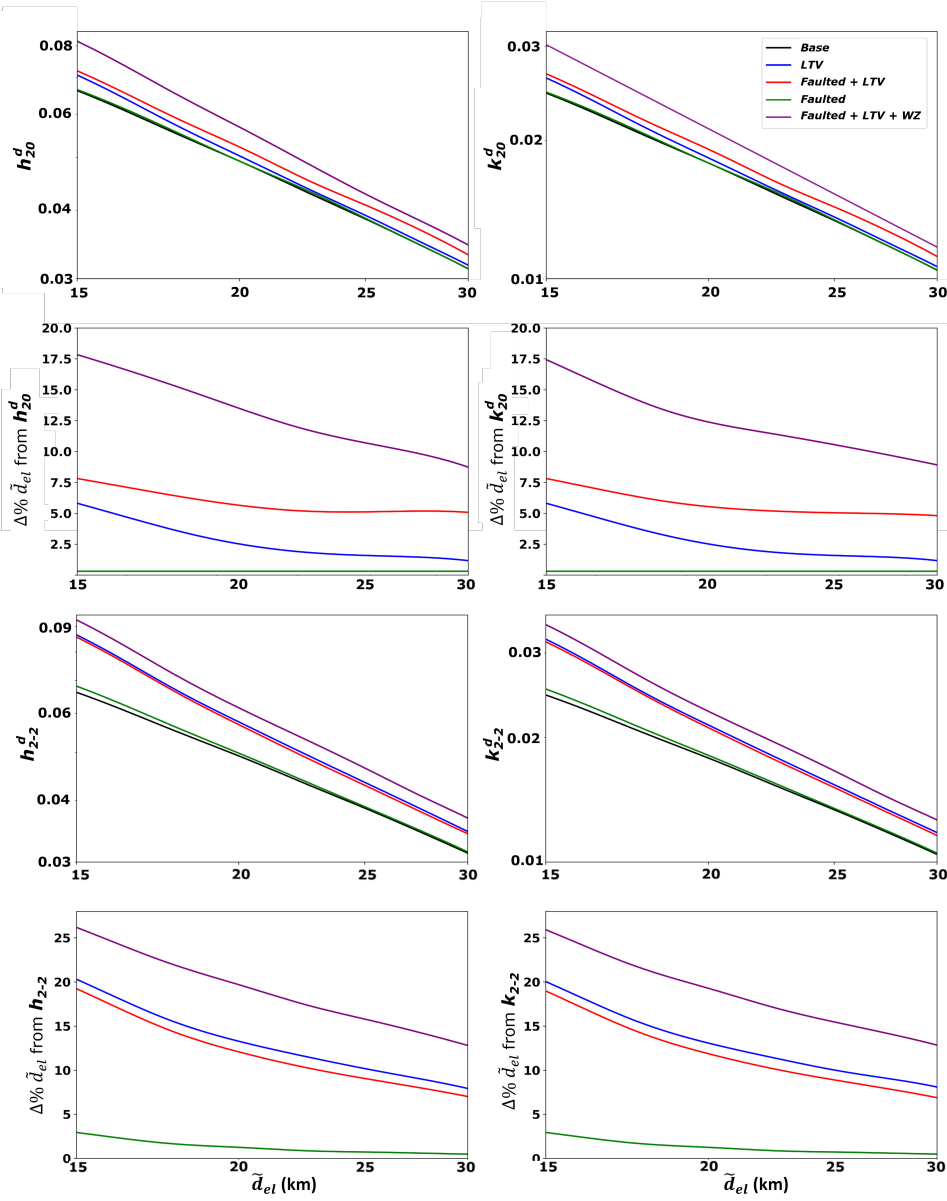


**Figure 4.** The relationship between deformation and mean effective elastic thickness,  $\tilde{d}_{el}$ .

First row:  $h_{20}^d$  and  $k_{20}^d$  vs.  $\tilde{d}_{el}$  for *Base* models (black lines), *LTV* models (blue lines), *Faulted* models (red lines), *Faulted+LTV* models (green lines), and *Faulted+LTV+WZ* (purple lines). We plot both axes in  $\log_{10}$  scale and generate curves by evaluating  $h_{20}^d$  and  $k_{20}^d$  at  $t=0$  (periapse) for 40 equally spaced  $\tilde{d}_{el}$  values between 15 and 30 km. Second row: Percentage range of  $\tilde{d}_{el}$  values corresponding to a fixed  $h_{20}^d$  and  $k_{20}^d$  value for each model category relative to the *Base* model. Curves in these plots are generated by evaluating the value of  $h_{20}^d$  and  $k_{20}^d$  corresponding to an  $\tilde{d}_{el}$  in the *Base* model (i.e.,  $\tilde{d}_b$ ), identifying the  $\tilde{d}_{el}$  value which maps to the same  $h_{20}^d$  and  $k_{20}^d$  values in models with structural heterogeneities (i.e.,  $\tilde{d}_{het}$ ) and evaluating  $\Delta\% \tilde{d}_{el} = 100 \cdot \frac{\tilde{d}_{het} - \tilde{d}_b}{\tilde{d}_b} \%$ .

X-axes are plotted in  $\log_{10}$  scale. Third and Fourth Rows: similar to first and second rows (respectively) but for  $h_{2-2}^d$  and  $k_{2-2}^d$  evaluated at  $t = \frac{\pi}{2\omega}$ .

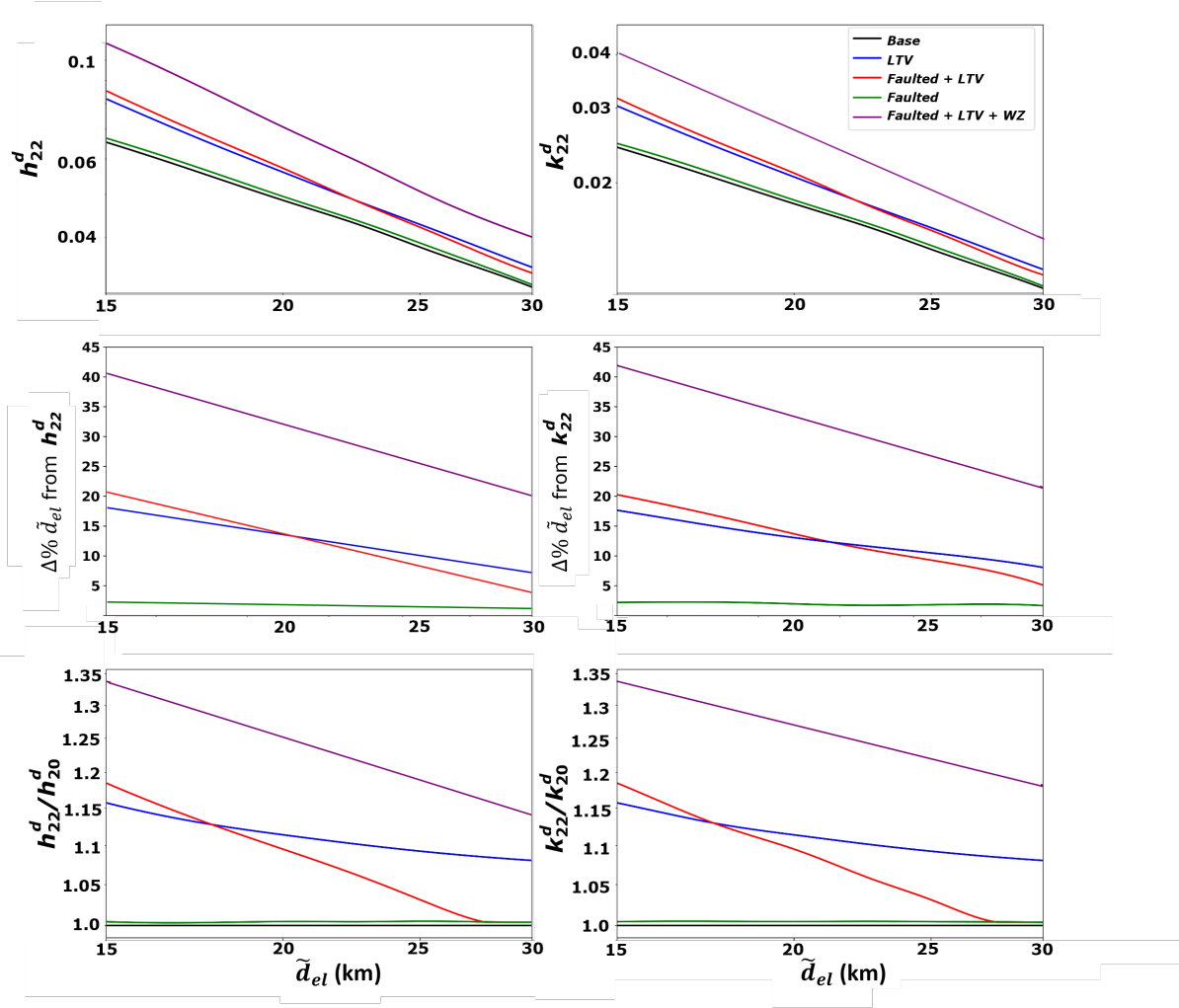


**Figure 5.** First row: Similar to first row of Figure 4 but for  $h_{22}^d$  and  $k_{22}^d$  instead of  $h_{20}^d$  and  $k_{20}^d$ . Second row: Similar to second row of Figure 4 for  $h_{22}^d$  and  $k_{22}^d$  instead of  $h_{20}^d$  and  $k_{20}^d$ . Third Row: ‘order-splitting’ associated with  $l = 2$  Love numbers. We evaluate  $k_{20}^d$ ,  $k_{22}^d$ , and  $k_{2-2}^d$  or  $h_{20}^d$ ,  $h_{22}^d$ , and  $h_{2-2}^d$  at  $t=0$  (periapse) for 40 equally spaced  $\tilde{d}_{el}$  values between 15 and 30 km to compute  $k_{22}^d/k_{20}^d$  and  $h_{22}^d/h_{20}^d$ . X-axes are plotted in  $\log_{10}$  scale.

ber values to decrease as maximum principal stresses rotate around the South Pole and fault slip decreases (see Figure 2).

Of the simplified structural heterogeneities considered, weak zones appear to have the most significant impact on the diurnal response of the ice shell to tides on Enceladus. The large spatial extent of the weak zones (i.e., 200–500 km in length or comparable to the radial length scale of Enceladus) and capacity to accommodate both additional normal- and shear-strain drives higher  $\tilde{d}_{el}$  values than those produced from the presence of variations in the thickness of the crust and faults in isolation. We find that for cases with less pronounced weak zones (i.e., where  $G_{WZ}/G > 10^{-5}$ ), the amplification of deformation drops dramatically (see Supplementary section S1.4 for details). These findings are consistent with results from Souček et al., (2016) and Behouňková et al., (2017) despite differences in the implementation of weak zones between the respective models (see section 2.4).

We find significant order-splitting (i.e.,  $k_{22}^d/k_{20}^d \neq 1$  and  $h_{22}^d/h_{20}^d \neq 1$ ) in models with structural heterogeneities. Moreover, Figures 1 and 5 suggest  $k_{22}^d/k_{20}^d$  and  $h_{22}^d/h_{20}^d$  are highly sensitive to the scale of non-spherically symmetric structure near the South Pole. For *LTV* models, radial displacement patterns exhibit strong, long-wavelength quadrupole symmetry about the south pole (i.e., generating an  $m = 2$  pattern) causing larger values of  $k_{22}^d/k_{20}^d$  and  $h_{22}^d/h_{20}^d$ . In contrast, slip along Tiger Stripe faults produces shorter-wavelength quadrupole deformation resulting in relatively smaller values of  $k_{22}^d/k_{20}^d$  and  $h_{22}^d/h_{20}^d$ . In *Faulted+LTV* models, slip-induced short wavelength deformation dominantly accommodates strain when  $\tilde{d} > 25$  km (i.e., resulting in  $k_{22}^d/k_{20}^d$  values trending towards 1, whereas at smaller values of  $\tilde{d}_{el}$ , the effect of LTVs dominate such that  $k_{22}^d/k_{20}^d$  and  $h_{22}^d/h_{20}^d \gg 1$ ). Weak zones produce the highest levels of quasi-quadrupole deformation near the South Pole and so drive the largest values of  $k_{22}^d/k_{20}^d$  and  $h_{22}^d/h_{20}^d$ .

The predicted amplitude of tidally-driven radial surface displacements falls within a readily measurable range at Enceladus. According to Figures 1, 4, and 5 radial surface displacement exhibits a maximum amplitude of about 50–150 cm and differences in maximal radial displacement amplitudes between models are about 5–20 cm. These values are substantially larger than the sensitivity of Interferometric Synthetic Aperture Radar (InSAR) measurements of ground displacement (e.g., Simons & Rosen, 2015). Moreover, surface displacements of 5–20 cm can induce 2–80  $\mu\text{Gal}$  gravity anomalies which



is greater than the expected detection limit of gravity measurements acquired from line-of-sight tracking between multiple orbiting spacecraft (e.g., Ramillien et al., 2004 and Dai et al., 2016). As such, a dedicated geodetic mission to Enceladus could be easily envisioned to make the measurements necessary for analysis of diurnal tides as discussed in this work.

We assume density structure for the crust and ocean (see Table 1), however the ocean density,  $\rho_w$ , is particularly uncertain. This uncertainty biases inferred values of  $\tilde{d}_{el}$  derived from diurnal Love numbers since  $\rho_w$  scales the restoring force at the ice-ocean interface (see section 2.2 and supplementary S1.1). Uncertainties in estimates of  $\rho_w$  are approximately 5% (i.e.,  $\rho_w = 1000\text{--}1050\text{ kg/m}^3$ ; Čadež et al., 2016) and thus uncertainty in  $\rho_w$  can modify diurnal Love numbers by up to 4%. Propagated uncertainty from imprecise estimates of  $\rho_w$  is therefore slightly larger than model uncertainty associated with the presence of Tiger Stripes (3%) but substantially smaller than that produced from neglecting the potential influence of weak zones or variations in ice shell thickness. Moreover, changing the input value of  $\rho_w$  should not produce order-splitting and so does not alter inferences short-wavelength shell structure from comparisons of diurnal Love numbers.

While we have focused on the relationship between diurnal Love numbers and  $\tilde{d}_{el}$  at Enceladus, a similar analysis could be done for Europa. In that case one should include the effect large-scale fault structures inferred from surface geology (e.g., Hoppa et al., 2000) but can exclude the effect of thickness variations due to the lack of significant non-hydrostatic topography (Nimmo et al., 2007). Ganymede, Callisto, and Titan do not exhibit large-scale crustal faulting and also apparently lack significant variations in outer ice shell thickness (McKinnon & Melosh, 1980; Cameron et al., 2019). As such, Enceladus appears to represent an extreme case where inferences of  $\tilde{d}_{el}$  from diurnal Love numbers are most ambiguous. Nonetheless, we demonstrate that analysis of diurnal tides could serve as a useful tool for characterizing interior structure from future geodetic investigations at ocean worlds.

## Open Research

This work utilizes the open-source finite element code Pylith (Aagaard et al., 2008) and the node-locked licensed software CUBIT (Skroch et al., 2019; CoreForm, 2020).

## Acknowledgments

This research was supported by the Future Investigators in NASA Earth and Space Science and Technology (FINESST) Program. We also thank the Keck Institute for Space Studies (KISS) at California Institute of Technology for organizing two workshops about “Next-Generation Planetary Geodesy” which provided insight, expertise, and discussions that greatly assisted the research. We also thank Matthew Knepley, Brad Aagaard, and Charles Williams for providing invaluable advice to modify Pylith for the simulations described this work. A portion of this research was supported by a Strategic Research and Technology Development task led by James T. Keane and Ryan S. Park at the Jet Propulsion Laboratory, California Institute of Technology, under a contract with the National Aeronautics and Space Administration (80NM0018D0004).

## References

- Aagaard, B., Williams, C., & Knepley, M. (2007). PyLith: A Finite-Element Code for Modeling Quasi-Static and Dynamic Crustal Deformation. *Eos*, *88*(52).
- Akiba, R., Ermakov, A. I., & Militzer, B. (2022). Probing the icy shell structure of ocean worlds with gravity–topography admittance. *The Planetary Science Journal*, *3*. doi: 10.3847/psj/ac4d2b
- Behouunkova, M., Soucek, O., Hron, J., & Cadec, O. (2017). Plume activity and tidal deformation on enceladus influenced by faults and variable ice shell thickness. *Astrobiology*, *17*(9). doi: 10.1089/ast.2016.1629
- Beuthe, M. (2018). Enceladus’s crust as a non-uniform thin shell: I tidal deformations. *Icarus*, *302*. doi: 10.1016/j.icarus.2017.11.009
- Cameron, M. E., Smith-Konter, B. R., Collins, G. C., Patthoff, D. A., & Papalardo, R. T. (2019). Tidal stress modeling of Ganymede: Strike-slip tectonism and Coulomb failure. *Icarus*, *319*. doi: 10.1016/j.icarus.2018.09.002
- CoreForm. (2020). ”CUBIT” <https://coreform.com/products/coreform-cubit/>.
- Dahlen, F. A., & Tromp, J. (1998). *Theoretical global seismology*. doi: 10.1063/1.882788
- Dai, C., Shum, C. K., Guo, J., Shang, K., Tapley, B., & Wang, R. (2016). Improved source parameter constraints for five undersea earthquakes from north component of GRACE gravity and gravity gradient change measurements. *Earth and Planetary Science Letters*, *443*. doi: 10.1016/j.epsl.2016.03.025

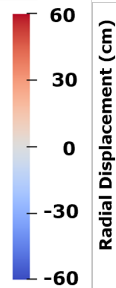
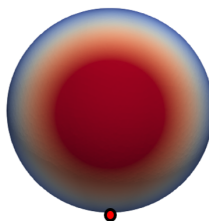
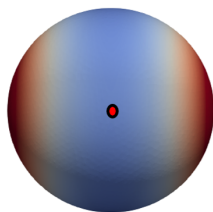
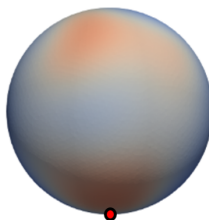
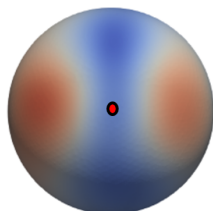
- 471 Ermakov, A. I., Park, R. S., Roa, J., Castillo-Rogez, J. C., Keane, J. T., Nimmo,  
472 F., ... Lainey, V. (2021). A recipe for the geophysical exploration of enceladus.  
473 *Planetary Science Journal*, 2. doi: 10.3847/PSJ/ac06d2
- 474 Goldreich, P. M., & Mitchell, J. L. (2010). Elastic ice shells of synchronous moons:  
475 Implications for cracks on europa and non-synchronous rotation of titan. *Icarus*,  
476 209. doi: 10.1016/j.icarus.2010.04.013
- 477 Hansen, C. J., Esposito, L., Stewart, A. I., Colwell, J., Hendrix, A., Pryor, W.,  
478 & Wast, R. (2006). Enceladus' water vapor plume. *Science*, 311. doi:  
479 10.1126/science.1121254
- 480 Hay, H. C., & Matsuyama, I. (2019). Nonlinear tidal dissipation in the subsurface  
481 oceans of enceladus and other icy satellites. *Icarus*, 319. doi: 10.1016/j.icarus  
482 .2018.09.019
- 483 Hemingway, D. J., & Matsuyama, I. (2017). Isostatic equilibrium in spherical coor-  
484 dinates and implications for crustal thickness on the Moon, Mars, Enceladus, and  
485 elsewhere. *Geophysical Research Letters*, 44(15). doi: 10.1002/2017GL073334
- 486 Hemingway, D. J., & Mittal, T. (2019). Enceladus's ice shell structure as a window  
487 on internal heat production. *Icarus*, 332. doi: 10.1016/j.icarus.2019.03.011
- 488 Hoppa, G., Greenberg, R., Tufts, B. R., Geissler, P., Phillips, C., & Milazzo, M.  
489 (2000). Distribution of strike-slip faults on Europa. *Journal of Geophysical Re-*  
490 *search E: Planets*, 105(E9). doi: 10.1029/1999JE001156
- 491 Hubbard, W. B., & Anderson, J. D. (1978). Possible flyby measurements of galilean  
492 satellite interior structure. *Icarus*, 33. doi: 10.1016/0019-1035(78)90153-7
- 493 Hurford, T. A., Helfenstein, P., Hoppa, G. V., Greenberg, R., & Bills, B. G. (2007).  
494 Eruptions arising from tidally controlled periodic openings of rifts on enceladus.  
495 *Nature*, 447. doi: 10.1038/nature05821
- 496 Iess, L., Stevenson, D. J., Parisi, M., Hemingway, D., Jacobson, R. A., Lunine, J. I.,  
497 & Tortora, P. (2014). The gravity field and interior structure of Enceladus.  
498 *Science*, 344(6179). doi: 10.1126/science.1250551
- 499 Ingersoll, A. P., Ewald, S. P., & Trumbo, S. K. (2020). Time variability of the ence-  
500 ladus plumes: Orbital periods, decadal periods, and aperiodic change. *Icarus*, 344.  
501 doi: 10.1016/j.icarus.2019.06.006
- 502 Jaccard, C. (1976). P. v. hobbs ice physics. oxford, clarendon press, 1974. xvii, 837  
503 p. £29. *Journal of Glaciology*, 17. doi: 10.3189/s0022143000030847

- 504 Kalyanaraman, B., Meylan, M. H., Bennetts, L. G., & Lamichhane, B. P. (2020). A  
 505 coupled fluid-elasticity model for the wave forcing of an ice-shelf. *Journal of Fluids*  
 506 *and Structures*, *97*. doi: 10.1016/j.jfluidstructs.2020.103074
- 507 Levinson, M. (1981). A new rectangular beam theory. *Journal of Sound and Vibration*, *74*. doi: 10.1016/0022-460X(81)90493-4
- 508  
 509 Love, A. E. H. (1909). The yielding of the earth to disturbing forces. *Proceedings of*  
 510 *the Royal Society of London. Series A, Containing Papers of a Mathematical and*  
 511 *Physical Character*, *82*. doi: 10.1098/rspa.1909.0008
- 512 McKinnon, W. B. (2015). Effect of enceladus’s rapid synchronous spin on  
 513 interpretation of cassini gravity. *Geophysical Research Letters*, *42*. doi:  
 514 10.1002/2015GL063384
- 515 McKinnon, W. B., & Melosh, H. J. (1980). Evolution of planetary lithospheres: Ev-  
 516 idence from multiringed structures on Ganymede and Callisto. *Icarus*, *44*(2). doi:  
 517 10.1016/0019-1035(80)90037-8
- 518 Melosh, H. J., & Raefsky, A. (1981). A simple and efficient method for introduc-  
 519 ing faults into finite element computations. *Bulletin of the Seismological Society of*  
 520 *America*, *71*(5). doi: 10.1785/bssa0710051391
- 521 Mitri, G., & Showman, A. P. (2005, 10). Convective–conductive transitions  
 522 and sensitivity of a convecting ice shell to perturbations in heat flux and  
 523 tidal-heating rate: Implications for Europa. *Icarus*, *177*(2), 447–460. doi:  
 524 10.1016/J.ICARUS.2005.03.019
- 525 Murray, C. D., & Dermott, S. F. (2000). *Solar System Dynamics*. doi: 10.1017/  
 526 cbo9781139174817
- 527 Neumeier, J. J. (2018). Elastic constants, bulk modulus, and compressibility of  
 528 h<sub>2</sub>o ice i h for the temperature range 50 k–273 k. *Journal of Physical and Chemi-*  
 529 *cal Reference Data*, *47*. doi: 10.1063/1.5030640
- 530 Nimmo, F., Bills, B. G., & Thomas, P. C. (2011). Geophysical implications of the  
 531 long-wavelength topography of the Saturnian satellites. *Journal of Geophysical*  
 532 *Research E: Planets*, *116*(11). doi: 10.1029/2011JE003835
- 533 Nimmo, F., Thomas, P. C., Pappalardo, R. T., & Moore, W. B. (2007). The global  
 534 shape of europa: Constraints on lateral shell thickness variations. *Icarus*, *191*. doi:  
 535 10.1016/j.icarus.2007.04.021
- 536 Porco, Dinino, D., & Nimmo, F. (2014). How the geysers, tidal stresses, and ther-

- mal emission across the south polar terrain of Enceladus are related. *Astronomical Journal*, 148. doi: 10.1088/0004-6256/148/3/45
- Porco, Helfenstein, P., Thomas, P. C., Ingersoll, A. P., Wisdom, J., West, R., & Squyres, S. (2006). Cassini observes the active south pole of Enceladus. *Science*, 311. doi: 10.1126/science.1123013
- Ramillien, G., Cazenave, A., & Brunau, O. (2004). Global time variations of hydrological signals from GRACE satellite gravimetry. *Geophysical Journal International*, 158. doi: 10.1111/j.1365-246X.2004.02328.x
- Roberts, J. H., & Nimmo, F. (2008, 4). Tidal heating and the long-term stability of a subsurface ocean on Enceladus. *Icarus*, 194(2), 675–689. doi: 10.1016/J.ICARUS.2007.11.010
- Schenk, P. M. (2008). Cartographic and Topographic Mapping of the Icy Satellites of the Outer Solar System. *International Archives of the Photogrammetry, Remote Sensing and Spatial Information Sciences*, 37.
- Schenk, P. M., Clark, R. N., Howett, C. J. A., Verbiscer, A. J., & Waite, J. H. (2018). *Enceladus and the icy moons of Saturn*. doi: 10.2458/azu\_uapress\_9780816537075
- Schubert, G., Anderson, J. D., Travis, B. J., & Palguta, J. (2007). Enceladus: Present internal structure and differentiation by early and long-term radiogenic heating. *Icarus*, 188(2). doi: 10.1016/j.icarus.2006.12.012
- Segall, P. (2010). *Earthquake and volcano deformation*. doi: 10.5860/choice.48-0287
- Shaw, G. H. (1985). Elastic properties and equation of state of high pressure ice. *The Journal of Chemical Physics*, 84. doi: 10.1063/1.449897
- Simons, M., & Rosen, P. A. (2015). Interferometric Synthetic Aperture Radar Geodesy. In *Treatise on geophysics: Second edition* (Vol. 3). doi: 10.1016/B978-0-444-53802-4.00061-0
- Skroch, M., Owen, S., Staten, M., Quadros, R., Hanks, B., Clark, B., & Stimpson, C. (2019). *CUBIT Geometry and Mesh Generation Toolkit 15.4 User Documentation*.
- Souček, O., Běhouňková, M., Čadek, O., Hron, J., Tobie, G., & Choblet, G. (2019). Tidal dissipation in Enceladus' uneven, fractured ice shell. *Icarus*, 328. doi: 10.1016/j.icarus.2019.02.012
- Souček, O., Hron, J., Běhouňková, M., & Čadek, O. (2016). Effect of the tiger

- 570 stripes on the deformation of Saturn’s moon Enceladus. *Geophysical Research*  
 571 *Letters*, *43*(14). doi: 10.1002/2016GL069415
- 572 Spencer, J. R., Pearl, J. C., Segura, M., Flasar, F. M., Mamoutkine, A., Romani,  
 573 P., & Lopes, R. M. (2006). Cassini encounters enceladus: Background and the  
 574 discovery of a south polar hot spot. *Science*, *311*. doi: 10.1126/science.1121661
- 575 Thomas, P. C., Tajeddine, R., Tiscareno, M. S., Burns, J. A., Joseph, J., Loredó,  
 576 T. J., & Porco, C. (2016). Enceladus’s measured physical libration requires a  
 577 global subsurface ocean. *Icarus*, *264*. doi: 10.1016/j.icarus.2015.08.037
- 578 Tyler, R. H. (2020). Heating of enceladus due to the dissipation of ocean tides.  
 579 *Icarus*, *348*. doi: 10.1016/j.icarus.2020.113821
- 580 Vance, S., Behoukova, M., Bills, B. G., Byrne, P., Cadek, O., Castillo-Rogez, J., ...  
 581 Wang, S. (2021). Distributed geophysical exploration of enceladus and other ocean  
 582 worlds. *Bulletin of the AAS*, *53*. doi: 10.3847/25c2cfcb.a07234f4
- 583 Wahr, Selvans, Z. A., Mullen, M. E., Barr, A. C., Collins, G. C., Selvans, M. M., &  
 584 Pappalardo, R. T. (2009). Modeling stresses on satellites due to nonsynchronous  
 585 rotation and orbital eccentricity using gravitational potential theory. *Icarus*,  
 586 *200*(1). doi: 10.1016/j.icarus.2008.11.002
- 587 Wahr, Zuber, M. T., Smith, D. E., & Lunine, J. I. (2006). Tides on Europa, and  
 588 the thickness of Europa’s icy shell. *Journal of Geophysical Research E: Planets*,  
 589 *111*(12). doi: 10.1029/2006JE002729
- 590 Yin, A., & Pappalardo, R. T. (2015). Gravitational spreading, bookshelf faulting,  
 591 and tectonic evolution of the South Polar Terrain of Saturn’s moon Enceladus.  
 592 *Icarus*, *260*. doi: 10.1016/j.icarus.2015.07.017
- 593 Zolotov, M. Y., & Shock, E. L. (2004). A model for low-temperature biogeochem-  
 594 istry of sulfur, carbon, and iron on Europa. *Journal of Geophysical Research E:*  
 595 *Planets*, *109*(6). doi: 10.1029/2003JE002194
- 596 Čadek, O., Tobie, G., Van Hoolst, T., Lefèvre, A., Mitri, G., Běhouňková, M., &  
 597 Trinh, A. (2016). Enceladus’s internal ocean and ice shell constrained from  
 598 cassini gravity, shape, and libration data. *Geophysical Research Letters*, *43*. doi:  
 599 10.1002/2016GL068634

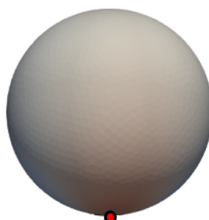
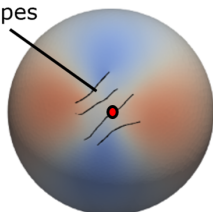
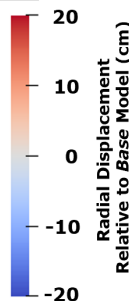
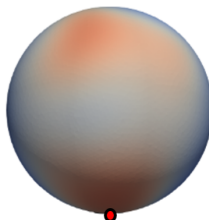
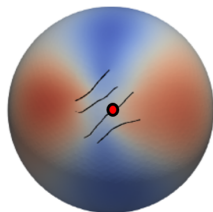
Figure 1.

**SP****SS*****Base******LTV***

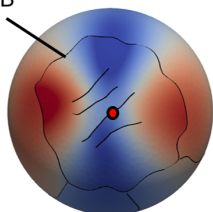
South Pole

***Faulted***

Tiger Stripes

***Faulted + LTV******Faulted + LTV + WZ***

CTB



chasma

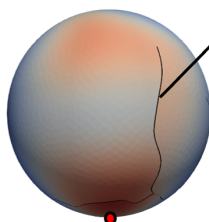
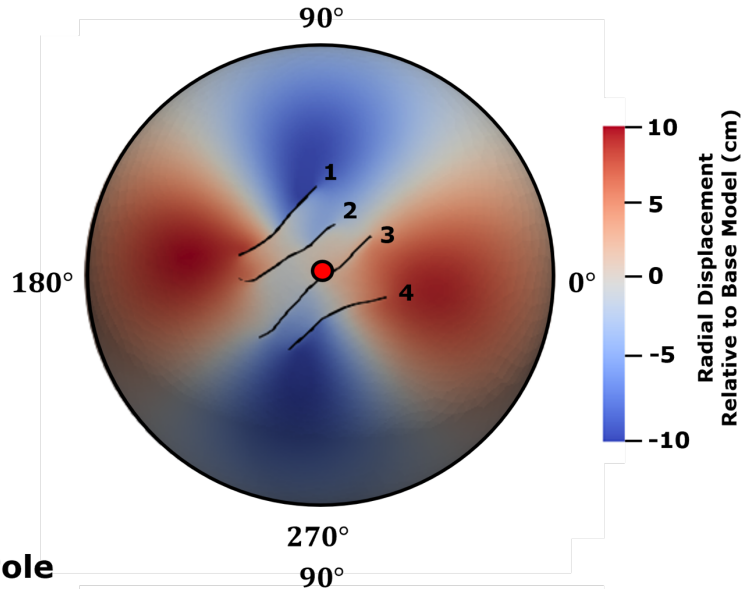
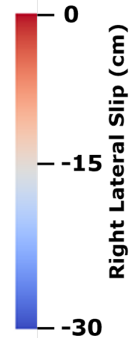
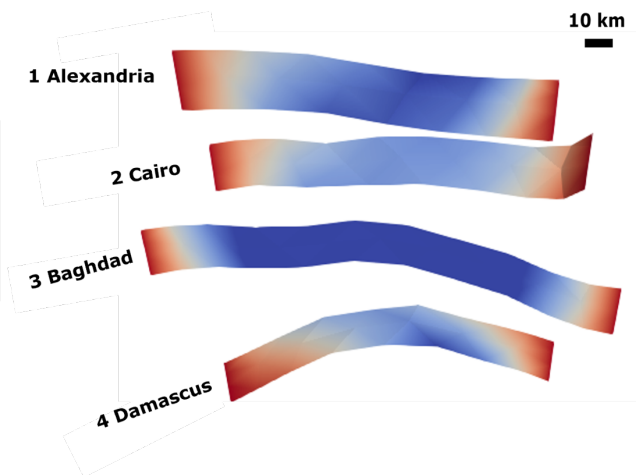




Figure 3.

**Faulted**



**LTV**

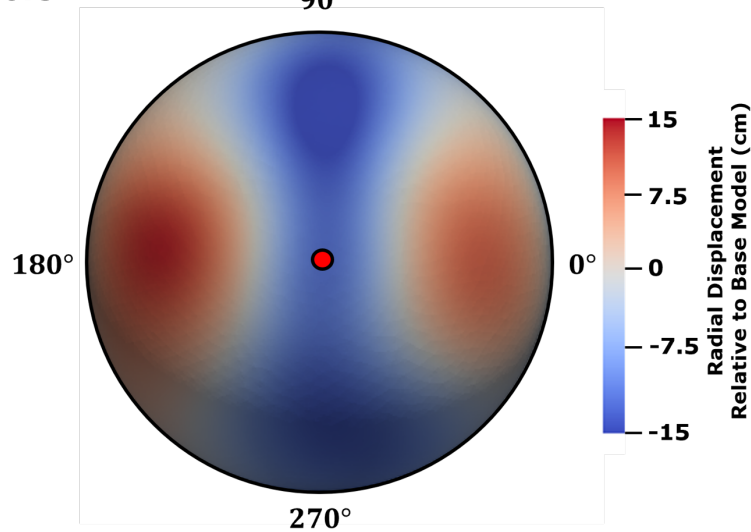
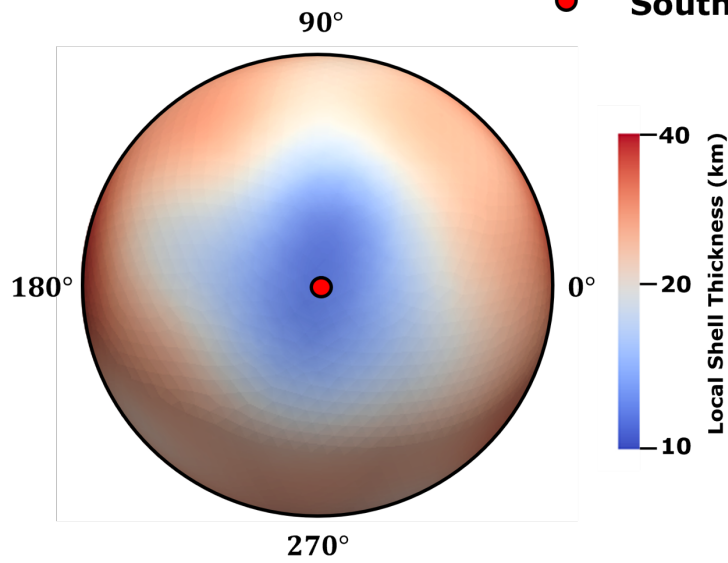


Figure 4.

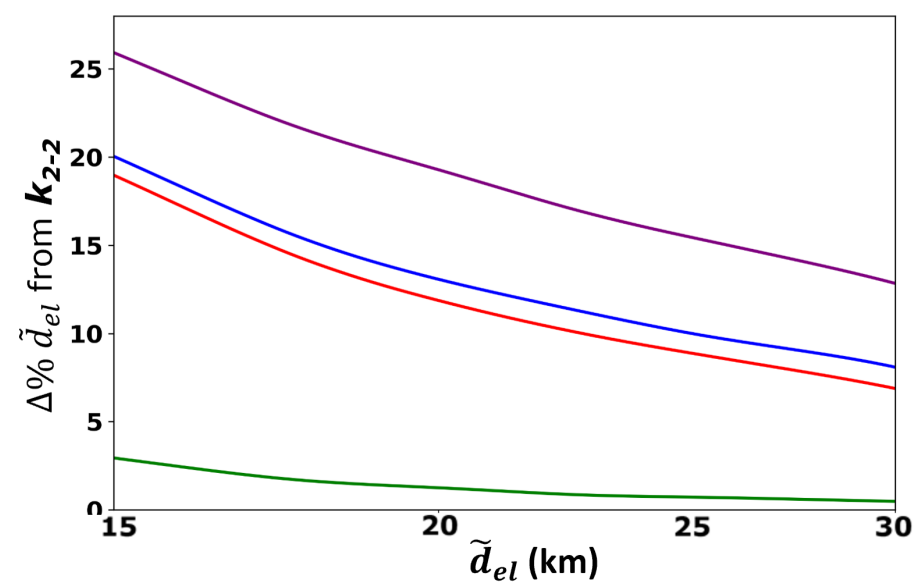
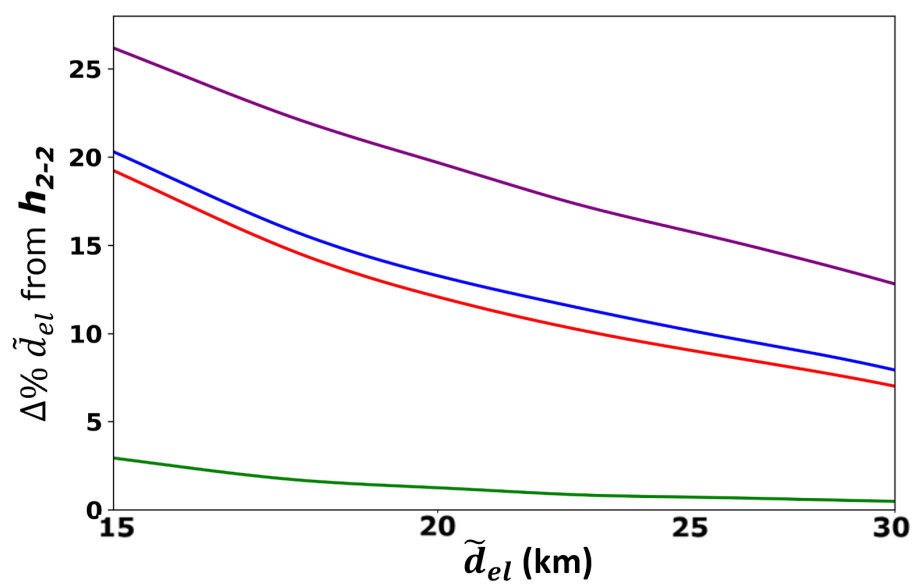
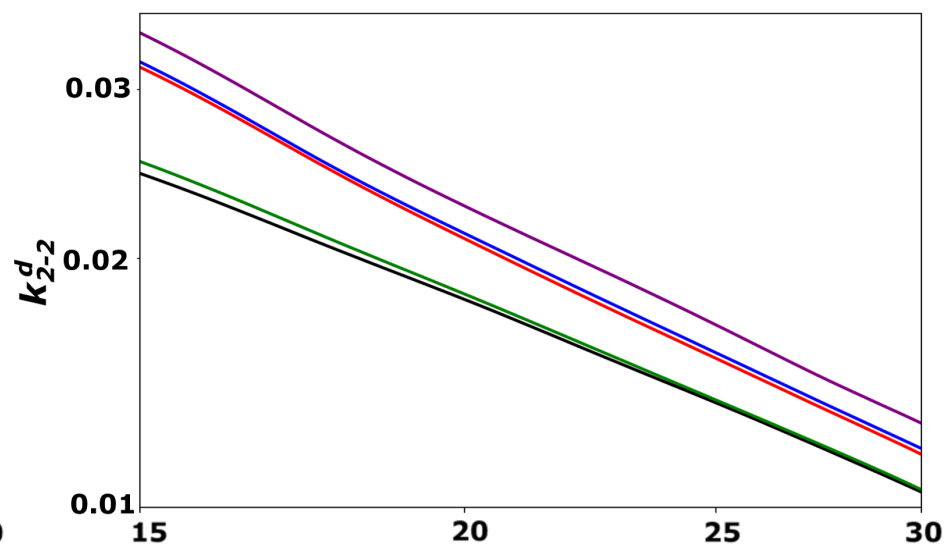
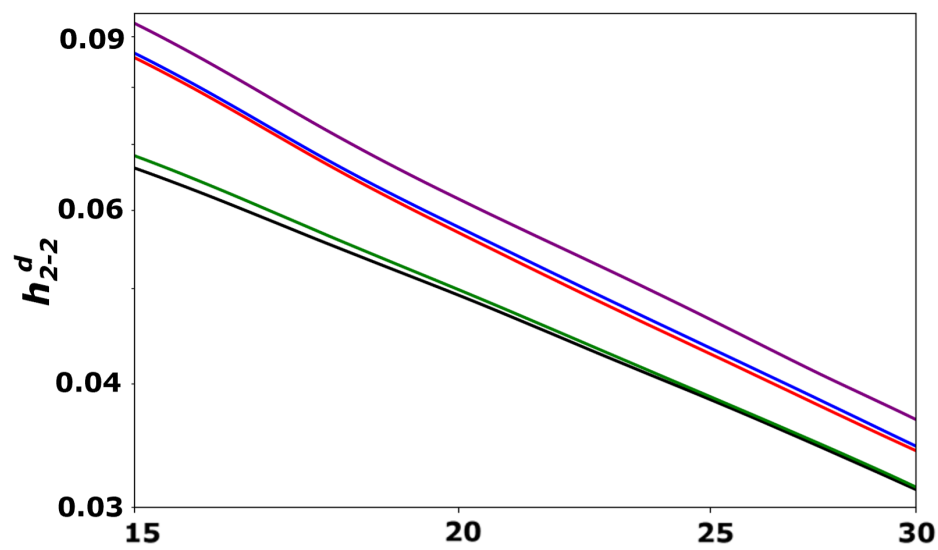
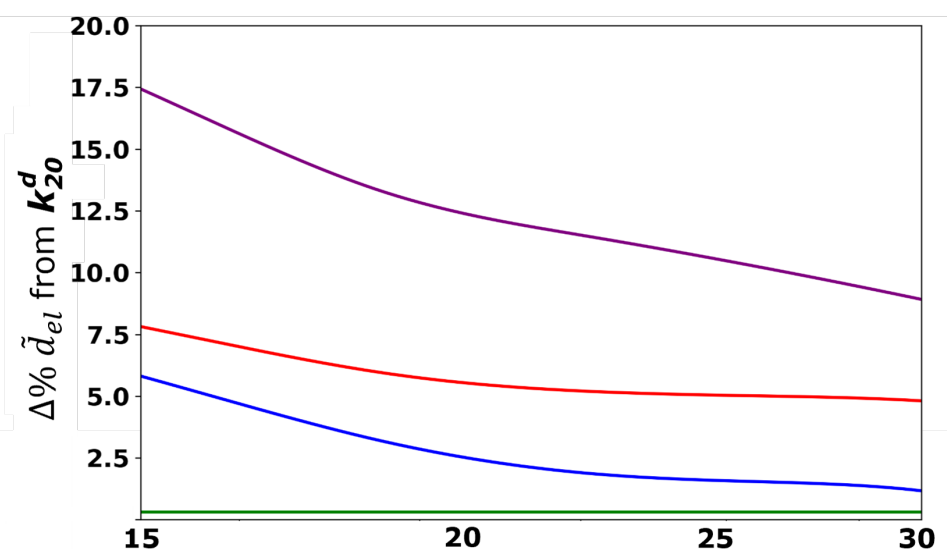
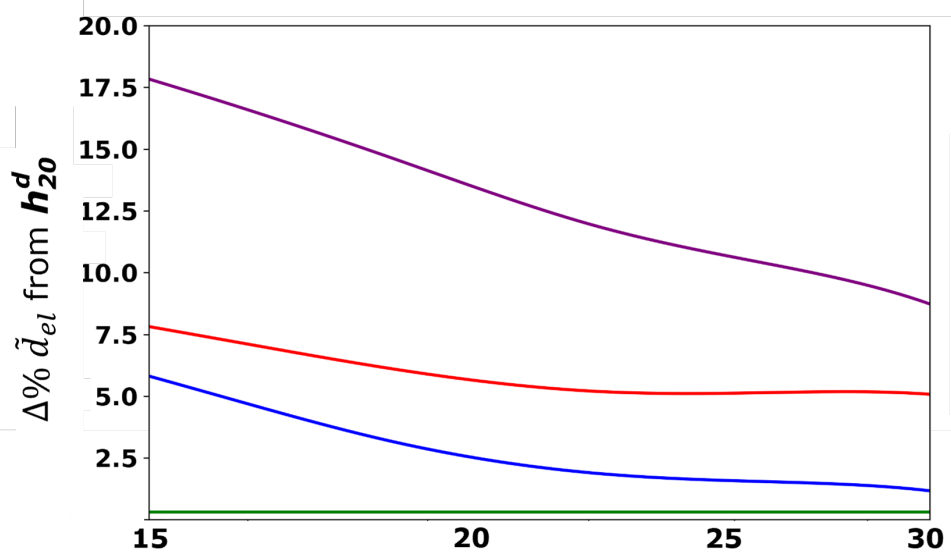
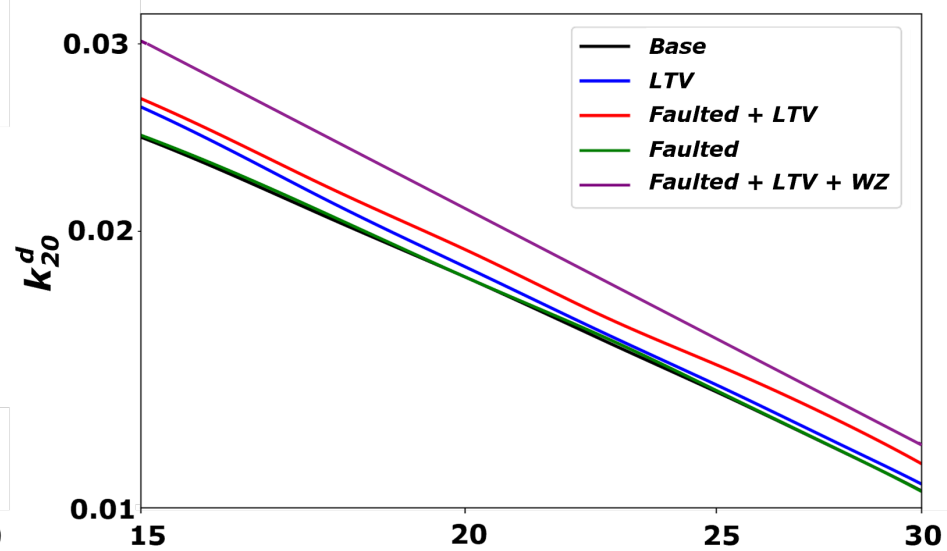
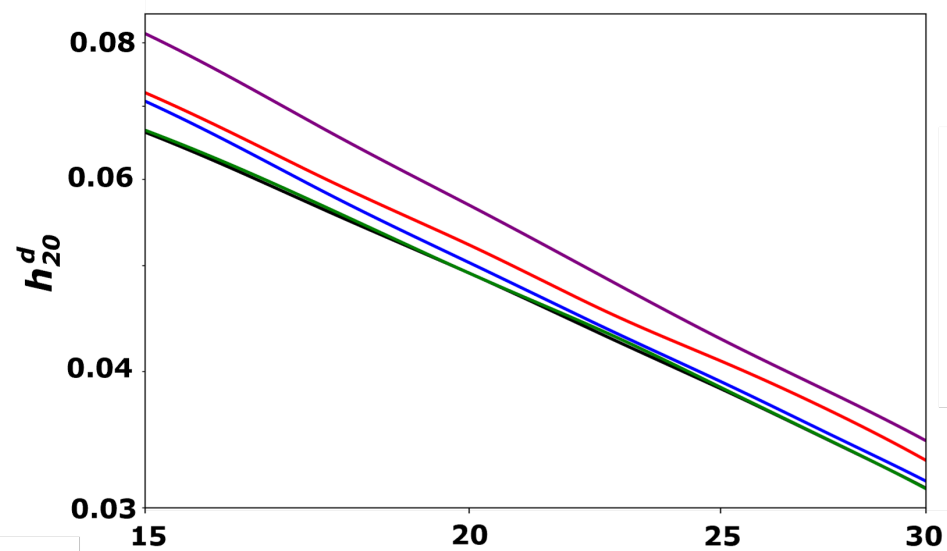
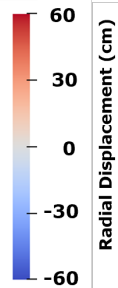
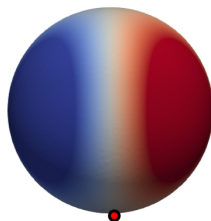
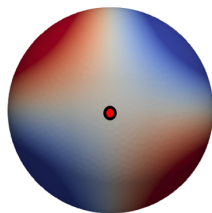
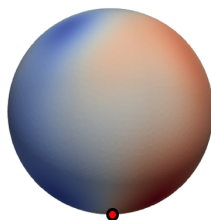
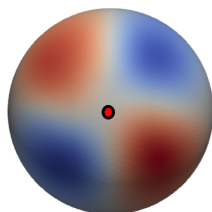


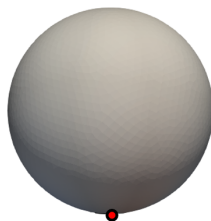
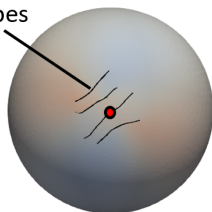
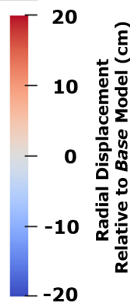
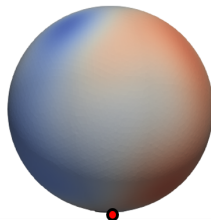
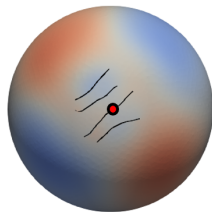
Figure 2.

**SP****SS****Base**

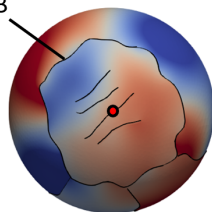
Radial Displacement (cm)

**LTV** South Pole

Tiger Stripes

**Faulted****Faulted + LTV**Radial Displacement  
Relative to Base Model (cm)**Faulted + LTV + WZ**

CTB



chasma

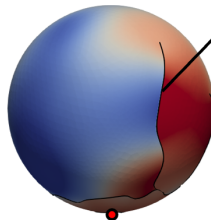


Figure 5.

